nature physics

Article

https://doi.org/10.1038/s41567-026-03205-7

Magnetic field-induced momentum-dependent symmetry breaking in a kagome superconductor

Received: 10 February 2025

Accepted: 2 February 2026

Published online: 11 March 2026

Check for updates

Jianwei Huang[1,2,15] ✉, Zheng Ren[1,2,15], Hengxin Tan[3], Jounghoon Hyun[1,2], Yichen Zhang[1,2], Thomas A. Hulse[1,2,4], Zhaoyu Liu[5], Jonathan M. DeStefano[5], Yaofeng Xie[1,2], Ziqin Yue[1,2,4], Junichiro Kono[1,2,6,7], Pengcheng Dai[1,2,8], Yu He[9], Aki Pulkkinen[10], Ján Minár[10], Jiun-Haw Chu[5], Ziqiang Wang[11], Binghai Yan[3,12], Rafael M. Fernandes[13,14] & Ming Yi[1,2,8] ✉

When several degrees of freedom in quantum materials have similar energy scales, the intertwined electronic orders, which exhibit broken symmetries, are often strongly coupled. Recent studies on kagome superconductors, such as CsV_3Sb_5, report rotational and time-reversal symmetry breaking linked to a charge density wave. Here we observe a momentum-selective response of the electronic structure of CsV_3Sb_5 to an external magnetic field. By performing angle-resolved photoemission spectroscopy in a tunable magnetic field, we demonstrate that the response of the electronic structure is compatible with piezomagnetism along with strong orbital selectivity. Our results show that the origin of the time-reversal symmetry breaking is associated with the vanadium Van Hove singularities at the onset of the charge-density-wave order. We also demonstrate the presence of fluctuations beyond the charge ordering temperature. Our results reveal that magnetic fields can be used as tuning knobs for disentangling intertwined orders in the momentum space for quantum materials.

The kagome lattice, a prototypical two-dimensional geometrically frustrated system, has been extensively studied as a promising candidate for realizing the quantum spin liquid state[1–3]. Beyond spin interactions, the kagome lattice also exhibits rich physics associated with the quantum interference of the electronic hopping paths. It hosts flat bands, Dirac cones and Van Hove singularities (VHSs) in its electronic structure[4–8]. When the flat bands or the VHSs are positioned near the Fermi level, electronic instabilities emerge, even for relatively weak electron–electron interactions, potentially leading to the emergence of different symmetry-breaking phases, such as magnetism, charge density wave (CDW), superconductivity and electronic nematicity[6–11]. Such a proximity to competing ordered states makes the kagome systems highly susceptible to external perturbations, such as a strain and magnetic fields, which could be used to tune the competition among the exotic phases[12–15]. Consequently, kagome metals provide an excellent platform for investigating the various intriguing symmetry-breaking phases due to the intricate interweaving among electron correlations, topology and geometric frustration[2,10,16].

CsV_3Sb_5 has been identified as a kagome superconductor ($T_c \approx 3.2$ K) with the V atoms forming the kagome lattice[17,18]. It undergoes a $2 \times 2 \times 2$ CDW transition at 94 K, which is captured well by first-principles calculations that indicate the relevant role of the electron–phonon coupling[19,20]. Interestingly, the CDW phase was also found to display unconventional properties indicative of time-reversal symmetry (TRS) breaking, which has been interpreted in terms of an interaction-driven loop-current phase[21–26]. These properties include

A full list of affiliations appears at the end of the paper. ✉e-mail: jwhuang0rice@gmail.com; mingyi@rice.edu

https://doi.org/10.1038/s41567-026-03205-7

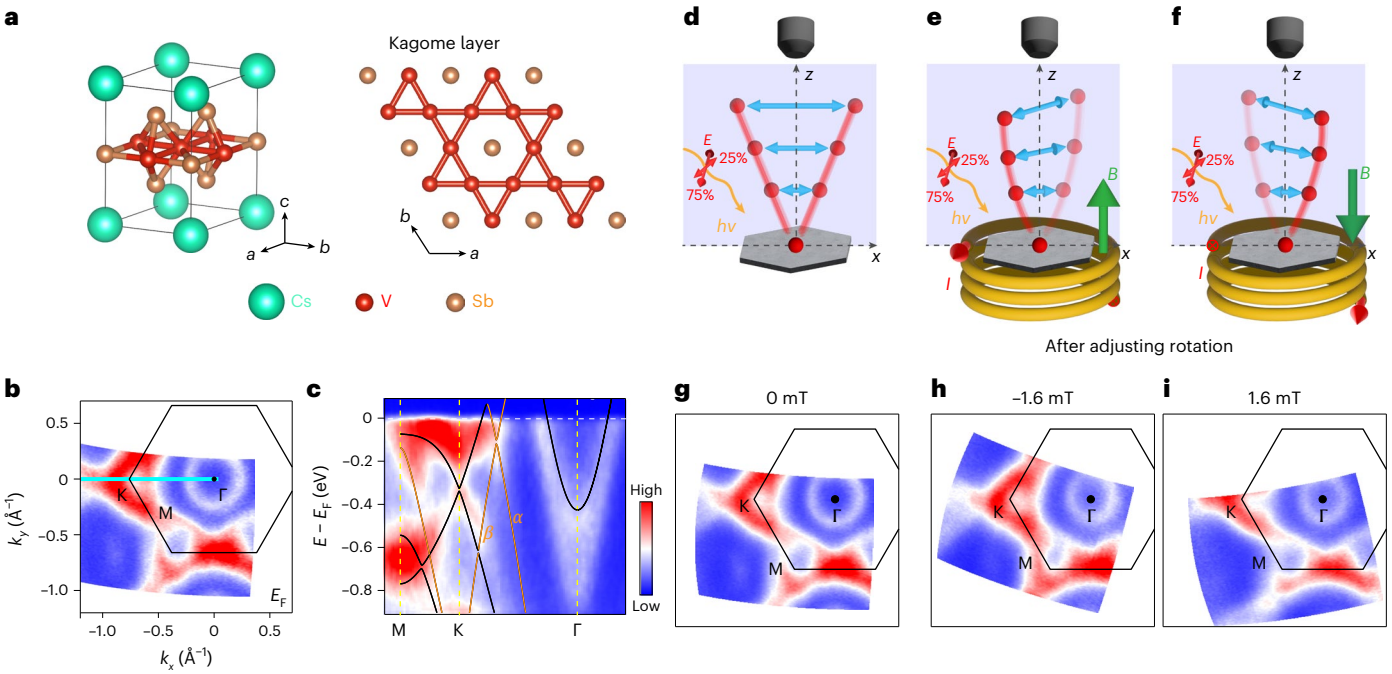

Fig. 1 | Magneto-ARPES experimental set-up and the measured electronic structure of CsV_3Sb_5. a, Crystal structure of CsV_3Sb_5. The V sublattice forms a kagome lattice. **b**, Measured Fermi surface of CsV_3Sb_5 in the absence of a magnetic field, obtained by rotating the sample relative to the analyser. k_x and k_y are the reciprocal axes of the corresponding x and y axes of the measurement geometry, where x and y are orthogonal. **c**, Spectral image extracted from the corresponding cut indicated in **b** overlaid with the DFT-calculated band dispersions. The bands labelled α and β respond most prominently to the external magnetic field, as revealed by magneto-ARPES. E_F represents the Fermi level. **d**, Schematic of the magneto-ARPES experimental geometry and photoelectron trajectory without an in situ magnetic field. **e**, Schematic of the magneto-ARPES experimental geometry and photoelectron trajectory with an in situ magnetic field generated by an electric current (I) through the solenoid coil on the sample stage. **f**, Same as **e** but with the electrical current and magnetic field reversed. The direction of the magnetic field B shown in **f** is defined as positive in this work. hv represents the photon energy. **E** represents the light polarization. **g**–**i**, The Fermi surfaces of CsV_3Sb_5 measured without (**g**) and with a magnetic field (−1.6 mT in **h** and 1.6 mT in **i**) illustrated in the configurations in **d**–**f**. Fermi surface rotations are corrected post-measurement.

an enhanced relaxation rate measured by muon spin rotation[27,28], magnetic-field switching of the relative intensity of the CDW Bragg peaks seen in scanning tunnelling microscopy[29,30], and anisotropic and non-reciprocal electrical magneto-transport[31–33]. On the other hand, the presence of non-zero magnetization remains under debate, in view of contradictory reports on the existence of a spontaneous Kerr effect[34–37]. Additionally, sixfold (C_6) to twofold (C_2) rotational symmetry breaking was detected at around 35 K in the CDW state of CsV_3Sb_5 by a combination of nuclear magnetic resonance and elastoresistance measurements[38]. This rotational symmetry breaking was attributed to the interlayer stacking of the $2 \times 2 \times 2$ CDW order[20] and interpreted as an electronic nematic order[39,40]. Although the interpretation in terms of nematic order has been challenged by recent studies that did not find a divergent nematic susceptibility[41], various experimental probes in CsV_3Sb_5, including polarization-resolved Raman spectroscopy[42], scanning tunnelling microscopy[43–45] and optical spectroscopy[34], have consistently found rotational symmetry breaking within the CDW state. Interestingly, resistivity anisotropy[33] and magnetic torque measurements[46] of CsV_3Sb_5 indicate that there may be a connection between rotational symmetry breaking and TRS breaking. Thus, to advance the understanding of this material and shed light on these conflicting experimental reports, a direct momentum-resolved spectroscopy measurement in the presence of a magnetic field is desirable.

In light of this, we used our recently developed angle-resolved photoemission spectroscopy with an in situ tunable magnetic field (magneto-ARPES)[47] to directly measure the response of the momentum-resolved electronic structure of CsV_3Sb_5 to an out-of-plane tunable magnetic field. ARPES has been notably successful in directly probing the momentum-resolved electronic spectra of quantum materials, and it provides a way to disentangle intertwined order parameters that exhibit distinct momentum-dependent fingerprints[48,49]. For the AV_3Sb_5 compounds (A = K, Rb or Cs), ARPES studies have revealed the key electronic characteristics inherent to the kagome lattice, along with the band folding and CDW gap associated with the CDW transition[50–53]. However, to date, no momentum-resolved electronic response to an external magnetic field has been reported using ARPES.

Magnetic fields are commonly used as tuning knobs in other types of experiments, but they have been carefully avoided in ARPES measurements due to their unpredictable effects on the photoelectron trajectory after photoemission[47,54]. Recently, we developed a simple method for implementing an in situ tunable out-of-plane magnetic field as the sample environment during ARPES measurements. The field is generated by a solenoid coil (Fig. 1e,f), thus enabling magneto-ARPES, a term coined by an independent group developing an in-plane field for ARPES[54]. Although the magnetic fields available in our set-up are small, below 10 mT, they are larger than the internal magnetic field values reported by the muon spin spectroscopy of AV_3Sb_5 (refs. 27,28). Using this capability, we performed magneto-ARPES measurements on CsV_3Sb_5 to probe the momentum-dependent electronic response to a magnetic field. Specifically, we observed spectral modifications to the dispersions and Fermi surfaces associated with the VHS bands of the vanadium d orbital around the K and K′ points of the Brillouin zone (BZ). Importantly, these spectral modifications broke the C_6 symmetry of the dispersion and were odd in the magnetic field, consistent with piezomagnetism[30]. Additionally, we observed an elliptical elongation of the electron pocket of the antimony p orbital around the Γ point of the BZ in the presence of a magnetic field. In contrast to the field-induced anisotropic spectral changes observed in the vanadium d bands, which

disappeared above the CDW transition temperature (T_{CDW}), the spectral changes around the Γ point persisted above T_{CDW}, indicating substantial fluctuations. Our magneto-ARPES results unambiguously reveal TRS breaking in CsV_3Sb_5. The TRS breaking was interwoven with rotational symmetry breaking and a qualitatively different magnetic-field response of the low-energy electronic states arising from the Sb *p* orbitals and the V *d* orbitals. These results not only provide strong constraints to theoretical delineations of the exotic CDW order parameter in CsV_3Sb_5, but they also establish a new capability for disentangling momentum-dependent order parameters in the presence of a field.

Field response of the V 3*d* VHS bands at K and K′

We first introduce the zero-field electronic structure of CsV_3Sb_5 measured using a helium lamp-based ARPES system (Fig. 1b,c; see Supplementary Section I for the measurement geometry). Consistent with previous reports, the Fermi surface of CsV_3Sb_5 is composed of a circular electron pocket around the BZ centre, consisting mainly of the 5*p* orbitals of Sb, and three triangles around the BZ corner (K and K′), consisting of the 3*d* orbitals of V and related to the nearby VHS at the M points[52,53]. The measured band dispersions match well with those obtained from calculations with density functional theory (DFT) (Fig. 1c).

Raw magneto-ARPES data generally consist of intrinsic effects that occur inside the sample in response to the magnetic field and extrinsic effects that occur when the field acts on the photoemitted electrons on their way to the analyser after they are ejected from the sample. The extrinsic effects consist of a rotation of the constant-energy contour due to the Lorentz force, photoelectron emission angle contraction and momentum broadening[47] (Fig. 1d–f). Specifically, for the small magnetic field adopted in this work (~1.6 mT), only a rotation of the constant-energy contour was discernible, as the other two effects were negligible[47] (Fig. 1g,h). This in-plane rotation of the constant-energy contour was effectively energy-independent within the energy range examined in this work (up to 1 eV below the Fermi level; Supplementary Section II), allowing straightforward post-measurement corrections without the need for intricate data-processing. It was also used to directly determine the field strength at the sample. As an example, Fig. 1g–i compares the Fermi surface mapped by rotating the sample measured at 0 mT, −1.6 mT and +1.6 mT. The maps display opposite rotation directions for positive and negative fields, which could be corrected by an in-plane azimuthal angle offset before any further data analysis was performed (Fig. 1h,i). To avoid any potential complications in field-dependent comparisons arising from the photoemission matrix-element effects[48], all subsequent measurements were performed with the DA30 deflector mode, so that we did not need to rotate or move samples when changing the magnetic field. Hence, in all comparisons with and without a field, the beam spot was kept on a fixed spot of the sample during the whole measurement, which guaranteed that the light polarization relative to the crystal axes remained the same when the field strength was changed.

We next compare the Fermi surface of CsV_3Sb_5 measured with and without a magnetic field in the CDW phase. To better observe the evolution of the electronic spectra in a magnetic field, we analysed the constant-energy contours at −0.35 eV, where the three sets of bands forming the triangular Fermi surfaces at the Fermi level (E_F) around K are well separated (Fig. 2a). In the absence of a magnetic field, two large triangular pockets (α and β) and a small circular pocket at K (K′) were resolved. The corresponding ARPES spectra were not distinguishable between K and K′ (Fig. 2b). Notably, the α and β sheets met at the M point and formed two sets of X-shaped constant-energy contours that straddle the M point across the two neighbouring BZs. When a magnetic field of 1.6 mT was applied, the overall shape of the constant-energy contour remained unchanged. However, one diagonal branch of the X-shaped sheets weakened into the spectral background whereas the other branch remained sharp and discernible (yellow arrow in Fig. 2c). Interestingly, when the direction of the magnetic field was reversed, the weakening of the X-shaped constant-energy contour also reversed between its two branches (yellow arrow in Fig. 2d).

To better illustrate this field-induced anisotropic spectral intensity change, *E*–*k* spectral images along cuts across both K and K′ were extracted for a side-by-side comparison (Fig. 2e–h and Extended Data Figs. 1 and 2). The cuts were taken perpendicular to the Γ–M mirror plane, where a mirror-symmetric spectral weight distribution was expected when there was no magnetic field. We note that the experimental geometry was chosen to preserve this mirror, as neither our beam polarization nor the incident direction breaks this mirror symmetry (Fig. 2). We focused on the α band, as its spectral weight was discernible over a large energy range. For cut 1 within the first BZ, the ARPES spectra of the α band on the left-hand side ($\alpha_{K'}$) and those of the α band on the right-hand side (α_K) of the $k_y = 0$ mirror plane were equivalent in the absence of a magnetic field (Fig. 2e). However, when an out-of-plane magnetic field (1.6 mT) was applied, the left branch of the α band intensity became 'weak' and the spectral weight became broader, as observed from the momentum distribution curve (MDC) in Fig. 2f. The spectral broadening reversed with respect to the horizontal mirror plane when the magnetic field direction was reversed (Fig. 2g). This can be better seen in the magneto-dichroic ARPES signal in Fig. 2h, which we define as the difference in spectral intensity between the two spectra obtained with magnetic fields with opposite directions and the same strength. This magneto-dichroic signal can be simulated well by a simple selective momentum broadening of ARPES spectra based on the DFT-calculated band structures along this cut (Extended Data Fig. 3). For cut 2, which lay outside the first BZ on the other side of the K–M–K BZ boundary, the opposite selective spectral weight broadening behaviour was observed between $\alpha_{K'}$ and α_K in a magnetic field compared with what was observed along cut 1 (Extended Data Fig. 1). The spectral evolution of the *E*–*k* images along both cuts 1 and 2 in an external magnetic field together complements the spectral response of the X-shaped energy isosurface to a magnetic field, which directly breaks the Γ–M mirror symmetry of the electronic states. We emphasize that this observation is an intrinsic electronic response of CsV_3Sb_5 to the external magnetic field, as the extrinsic momentum broadening effect is negligible at this small field and should be neither momentum selective nor dependent on the sign of the field[47].

To pinpoint the precise symmetries that are broken by this anisotropic effect, we note that our measurement region also covers part of the second BZ, which we mapped back to the first BZ via the crystalline translational symmetry. We directly verified this by rotating the sample and mapping the response of different K and K′ pairs to the magnetic field on the same sample (Extended Data Fig. 4). This led to the illustration in Fig. 2i, where the broadened branches of the Fermi surface are depicted by the thicker and lighter-coloured lines and the sharper branches are represented by the thinner and darker-coloured lines. Comparing the behaviour of the branches across the first BZ, we conclude that the inversion symmetry was preserved, whereas the sixfold (C_6) rotational symmetry was broken. Moreover, as the effect changed sign when the field was reversed, the rotational symmetry breaking was odd in the field, which is indicative of piezomagnetism, namely a shear strain that is linear with the field[30].

To further explore this effect, we performed temperature-dependent measurements of the *E*–*k* spectral images of CsV_3Sb_5 at a fixed magnetic field (Fig. 2j–n and Supplementary Section III). Although the cut position (cut 3) slightly deviated from cut 1 in Fig. 2b, it still captured both the $\alpha_{K'}$ and α_K bands (Fig. 2j). As the temperature was increased, the originally asymmetric $\alpha_{K'}$ and α_K bands in the CDW state regained their symmetry at higher temperatures. This is evident from the corresponding MDCs shown for −0.42 eV. Although the two peaks had distinct widths at 20 K, they gradually returned to having similar widths at higher temperatures (Fig. 2k). This evolution is also visualized by the corresponding false-colour map generated from the stacking of the temperature-dependent MDCs (Fig. 2l). We quantified this

https://doi.org/10.1038/s41567-026-03205-7

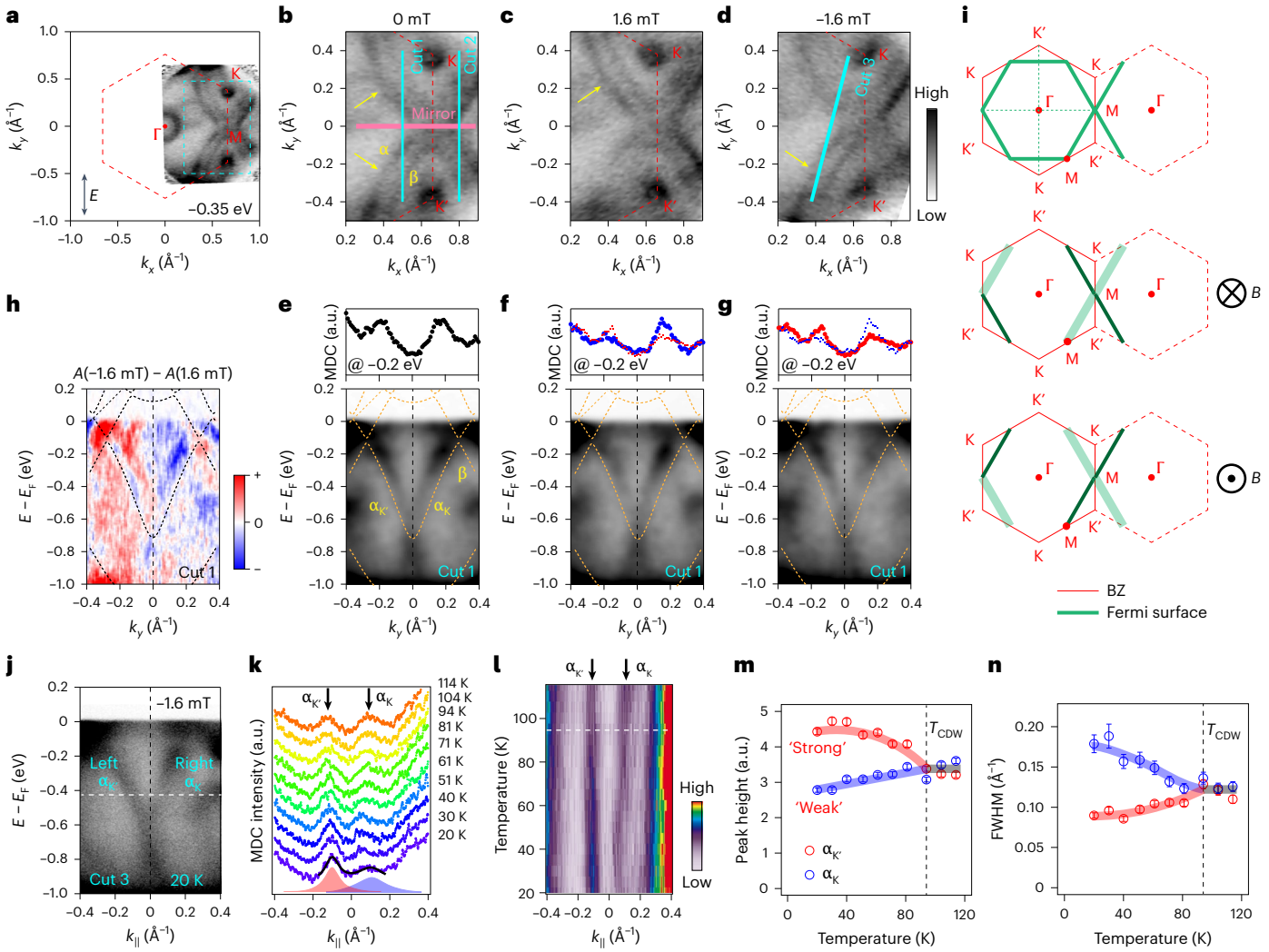

Fig. 2 | Field response of the electronic states originating from the V *d* orbitals near K and K′. **a**, Constant-energy contour of CsV_3Sb_5 at −0.35 eV measured without a magnetic field using DA30 mode. The double-headed arrow indicates the dominant light polarization. **b**, Zoomed-in view of the dashed cyan rectangle in **a**. The yellow arrows point to the sharp electronic sheets around both K and K′. **c**, Same as **b** but in the presence of a magnetic field of +1.6 mT. The yellow arrow points to the electronic sheets that remain sharp around K. **d**, Same as **b** but in the presence of a magnetic field of −1.6 mT. The yellow arrow points to the electronic sheets that remain sharp around K′. **e**–**g**, *E*–*k* spectral images and the related MDCs at −0.2 eV along cut 1 indicated in **b**, corresponding to the measurements under a magnetic field of 0 mT (**e**), +1.6 mT (**f**) and −1.6 mT (**g**). The yellow dashed lines overlaid are the corresponding DFT band dispersions. **h**, The magneto-dichroic spectral image obtained by subtracting **f** from **g**. The black dashed lines overlaid are the DFT band dispersions. **i**, Schematics showing the VHS Fermi surfaces without and with a magnetic field. The thicker and fainter lines indicate broadened branches, and thinner and more intense lines represent sharper branches. **j**, Spectral images taken along cut 3 marked in **d** measured at −1.6 mT and 20 K. **k**, MDCs taken at −0.42 eV as marked in **j** and measured at various temperatures. The fitted peaks for $\alpha_{K'}$ and α_K bands measured at 20 K are shown as shaded peaks. **l**, Spectral image obtained by combining the MDC stacks in **k**. **m**,**n**, Fitted peak height (**m**) and peak width (**n**) of $\alpha_{K'}$ and α_K as functions of temperature. The error bars in **m** and **n** represent the standard deviations from the 95% confidence interval of Lorentzian fits to the corresponding MDC peaks in **k**. The centres of the error bars represent the corresponding fitted results. FWHM, full-width at half-maximum.

temperature dependence by fitting both the peak height and peak width of $\alpha_{K'}$ and α_K from the MDCs. As seen from the resulting plots (Fig. 2m,n), both the peak intensity and width became asymmetric below T_{CDW}, indicating that the symmetry breaking associated with the vanadium VHS bands is intrinsically linked to the CDW order.

Having demonstrated the magnetic-field-induced C_6 symmetry breaking of the electronic spectrum in the CDW state of CsV_3Sb_5, we examined in detail the evolution of its spectral weight as a function of magnetic field (Fig. 3 and Supplementary Section III). The *E*–*k* spectral images along the Γ–K′ direction measured at different magnetic fields were obtained as a cut from the Fermi surface mappings using the DA30 deflector mode after correcting for the Lorentz rotation (Fig. 3a). In this measurement geometry, the aforementioned α band is suppressed whereas the β band acquired a clearer resolution. As expected from our analysis of the α band, the spectral weight of the β band substantially broadened under a positive magnetic field (2.1 mT), whereas the effect on the other bands was much less noticeable. To quantify this evolution, we extracted the MDCs at −0.2 eV from the Γ–K′ spectral images (Fig. 3b). Three distinct peaks (P1, P2 and P3) were resolved. P1 originated from the electron band around the BZ centre, P3 from the shallow Dirac point at K′ and P2 from the β band. As the out-of-plane magnetic field was varied from negative to positive, peak P2 (β band) broadened substantially in comparison with the linewidths of peaks P1 and P3 (Fig. 3d and top row of Fig. 3a). The evolution of the peak area followed a similar trend, although varying less in comparison with the peak width.

The odd-in-field response of the electronic structure to the out-of-plane field is an indication of TRS breaking. To understand

https://doi.org/10.1038/s41567-026-03205-7

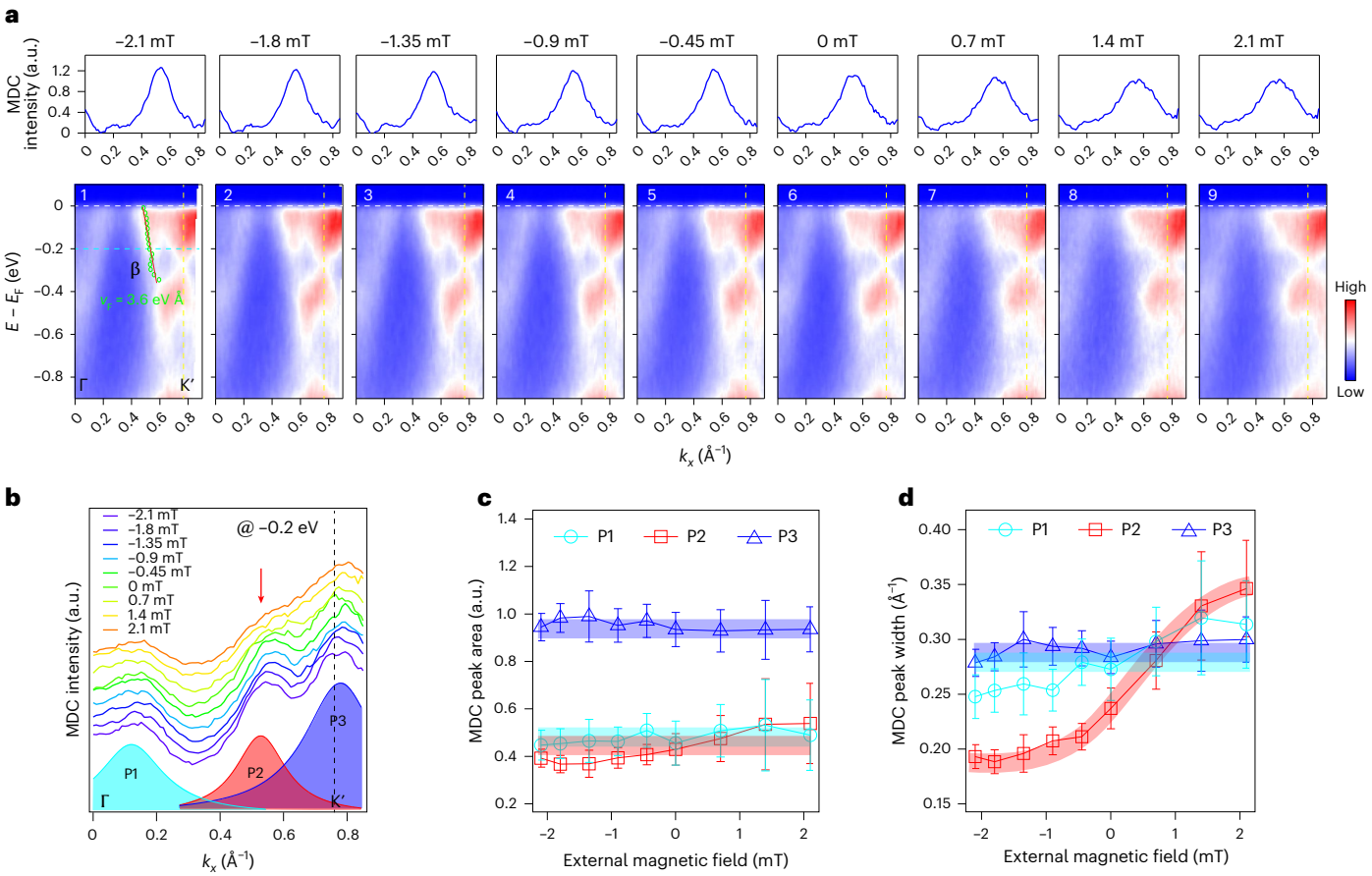

Fig. 3 | Magnetic field dependence of the electronic spectrum near K. **a**, Spectral images along the Γ–K′ direction at different external magnetic fields. The top row shows the corresponding P2 peaks indicated in **b** after subtracting the fitted background and other peaks from the MDCs. **b**, Corresponding MDCs at −0.2 eV of the spectral images in **a** at different magnetic fields. The red arrow points to the peak (P2) from the β band, which responded most prominently to the magnetic field. The α band was strongly suppressed in this measurement geometry due to matrix-element effects. The MDCs were fitted by three Lorentzian peaks (P1, P2 and P3) and a fixed constant background. **c**, The fitted MDC peak areas as a function of magnetic field for the three corresponding peaks in **b**. **d**, The fitted MDC peak widths as a function of magnetic field for the three corresponding peaks in **b**. The error bars represent the standard deviations of the Lorentzian fits to the MDC peaks in **b** with 95% confidence intervals. The centres of the error bars represent peak areas (**c**) and peak widths (**d**) obtained from Lorentzian fits.

the origin of the observed asymmetric spectral shape under a magnetic field, we carried out one-step model ARPES calculations using the spin-polarized relativistic Korringa–Kohn–Rostoker package to examine the effect of an external magnetic field on the photoemission spectral function of CsV_3Sb_5 (ref. 55; Methods and Extended Data Fig. 5). By calculating the spectral function of the non-CDW phase of CsV_3Sb_5 under an external field, we simulated the photoemission spectra under a finite field for the simplest phase with TRS broken via the Zeeman effect without invoking a specific microscopic TRS-broken order. This set of calculations incorporates the effects of a magnetic field in all three parts of the photoemission matrix element: a Zeeman term for the initial state, the relativistic dipole operator and the time-reversed spin-polarized low-energy electron diffraction final states. It is, hence, the simplest yet most unbiased way to examine the expectations from a generic TRS-broken state. As shown in Extended Data Fig. 5, the spectra near the K and K′ points exhibited an asymmetric spectral shape, for both peak heights and widths, when photoemitting under a large magnetic field. This was due to the combination of the field-induced band shift and spin-dependent multiple scattering during the photoemission process under a particular field direction. Although at first sight this may seem consistent with our observations, the magnitude of the field needed for the Zeeman effect to be observable is five orders of magnitude larger than the field used in the magneto-ARPES measurements. Hence, the electronic response experimentally observed here could not have arisen from a Zeeman-like field-induced effect on the photoemission matrix elements but must have originated from an intrinsic TRS-breaking order parameter in CsV_3Sb_5.

Field response of the Sb 5*p* band at Γ

Next, we turn our attention to the electron pocket around the BZ centre (Fig. 4), which arises from the Sb *p* orbitals. When measured at zero field, as consistent with all previous reports[50–53], the central electron pocket was nearly isotropic and circular inside the CDW state (Fig. 4a). This is demonstrated by comparing the MDC along the vertical Γ–K and horizontal Γ–M directions, which shows that the separations of the two peaks are identical along the two orthogonal directions (Fig. 4b). However, when an out-of-plane magnetic field of −1.6 mT was applied, the circular Fermi pocket became elliptical (Fig. 4e), as can also be seen in the same comparison of the vertical (black) and horizontal (red) MDCs (Fig. 4f). Our extensive simulations demonstrate that we can exclude the possibility that this distortion of the Fermi surface was due to potential misalignment between the sample and the magnetic coil, the ellipticity of the beam, or the spatial inhomogeneity of the field (Supplementary Sections IV, V and VI). Rather, the elliptical distortion of the central Fermi pocket under the application of a magnetic field indicates a field-induced rotational symmetry breaking in CsV_3Sb_5

https://doi.org/10.1038/s41567-026-03205-7

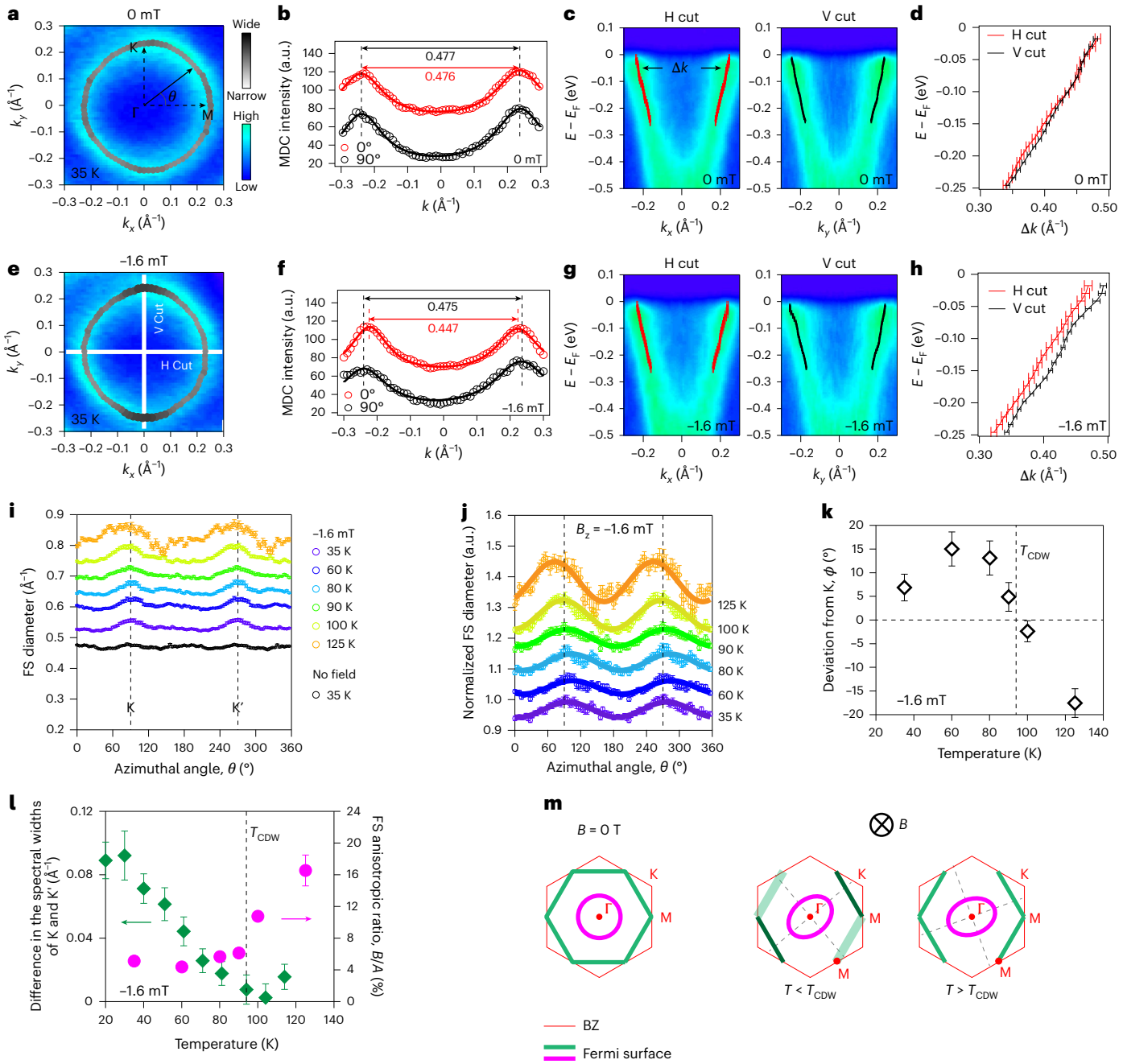

Fig. 4 | Field response of the electronic states originating from the Sb *p* orbitals near Γ. a, Measured Fermi surface around Γ in the absence of a magnetic field. The azimuthal angle θ is defined with respect to the horizontal Γ–M direction. **b**, MDC across the Fermi pocket along the horizontal ($\theta = 0°$) and vertical ($\theta = 90°$) directions, fitted by a two-Lorentzian function to extract the diameter measured along the two directions. **c**, Spectral images measured along the two orthogonal cuts, overlaid with the peak positions of the MDC fitting for the dispersions. **d**, The extracted momentum separation of the fitted dispersions in **c** as a function of energy. The error bars were obtained by taking the square root of the sum of squares of the standard deviations from the Lorentzian fits to the MDCs. **e**–**h**, Same as **a**–**d** but for measurements in a magnetic field of −1.6 mT. **i**, Fermi pocket diameter as a function of the azimuthal angle obtained by fitting the radial MDCs without and with a magnetic field at different temperatures. The curves are offset for clarity. Error bars are the standard deviations from the corresponding Lorentzian fits with 95% confidence intervals. **j**, Fermi pocket diameter under −1.6 mT and different temperatures normalized by its zero-field value measured at 35 K. Error bars were derived from **j**. All curves were fitted with the function $A + B\cos(2(\theta + \phi))$. **k**, The deviation of the long axis of the elliptical Fermi pocket away from the K point as a function of temperature at −1.6 mT. Error bars represent the standard deviation obtained from sinusoidal fits to the corresponding data in **j** with 95% confidence intervals. The centres of the error bars represent the angle between the fitted longitudinal direction and the Γ–M direction. **l**, Temperature dependence of the ellipticity of the Fermi pocket (solid diamonds) plotted together with the temperature evolution of the VHS spectral difference (solid circles), all measured at −1.6 mT. Error bars on the solid diamonds were obtained by taking the square root of the sum of squares of the corresponding error bars in Fig. 2n. Error bars on the solid circles represent the standard deviations obtained from sinusoidal fits to the corresponding data in **j** with 95% confidence intervals. **m**, Summary schematics of the temperature evolution of the field response of the electronic structure of CsV_3Sb_5. At zero magnetic field for any temperature, the Γ pocket is circular and the large Fermi surface associated with the VHS respects the C_6 symmetry. In the presence of a magnetic field, for $T < T_{CDW}$, the large Fermi surface breaks the C_6 rotational symmetry and the Γ pocket becomes elongated and rotates away from Γ–K. Just above T_{CDW}, the large Fermi surface restores the C_6 symmetry, but the Γ pocket retains its ellipticity. FS, Fermi surface; H, horizontal; V, vertical.

corresponding to broken C_6 symmetry. Beyond the Fermi surface, we also show the measured dispersions along the vertical and horizontal directions for both zero field and −1.6 mT (Fig. 4c,g). Their fits show that this elliptical distortion was not limited to the Fermi level but persisted to a larger energy range of at least 250 meV below the Fermi level (Fig. 4d,h).

Another way to assess this anisotropy is to extract the diameter of the fitted Fermi surface as a function of the azimuthal angle (θ). As shown in Fig. 4i, the ellipticity of the Fermi surface at −1.6 mT is prominent compared with that at zero field at various temperatures. This trend is better seen by plotting the angle-dependent diameter of the Fermi surface in a magnetic field normalized by its zero-field value (Fig. 4j). We note that this angle-dependent normalized diameter of the Fermi surface can be fitted well by a phenomenological function of the form $A + B\cos(2(\theta + \phi))$, which captures the twofold rotational symmetry, with B/A denoting the anisotropy ratio of the Fermi surface and the angle ϕ denoting the deviation of the long axis of the elliptical Fermi surface from the BZ high-symmetry Γ–M (Γ–K) direction. Intriguingly, we found that in the CDW phase in a magnetic field, the long axis of the elliptical Fermi surface deviated from the high-symmetry Γ–K direction of the BZ (Fig. 4j,k). Moreover, the directional deviation of the elliptical Fermi surface also changed with temperature, going through zero at T_{CDW} and reversing sign above T_{CDW} (Fig. 4k). Additionally, the amplitude of the ellipticity of the Fermi surface remained relatively constant below T_{CDW} and increased with increasing temperature above T_{CDW} (Fig. 4l). We plot the temperature dependence of the Γ pocket represented by the distortion of the Fermi surface together with the difference in the VHS spectral widths extracted previously (Fig. 4l). Their behaviours are distinct across T_{CDW}. The difference in the spectral widths of the V 3*d* VHS started below T_{CDW}. Moreover, the ellipticity of the Γ electron pocket was finite and largely constant below T_{CDW} but grew above T_{CDW} up to the measured temperature of 125 K (Fig. 4m).

Discussion

Our magneto-ARPES measurements reveal distinct field responses, inside the CDW phase, of the V 3*d* orbitals that make up the bands associated with the VHS of the kagome lattice and the Sb *p* orbitals that make up the band at the BZ centre. The odd-in-field response of the VHS bands breaks the C_6 rotational symmetry, thus implying that the CDW phase of CsV_3Sb_5 is piezomagnetic, namely, that an out-of-plane magnetic field induces an in-plane distortion. Piezomagnetism, which manifests the intrinsic coupling between TRS breaking and rotational symmetry breaking, was also inferred in a recent scanning tunnelling microscopy study on the related compound RbV_3Sb_5 (ref. 30), which attributed this response to a so-called congruent flux phase with coexisting CDW and loop-current order. In this state, the C_6 rotational symmetry is already weakly broken in the absence of a magnetic field, and the application of a magnetic field further breaks the remaining vertical mirror, leaving intact only the horizontal mirror. Our ARPES data at zero field, however, are C_6 symmetric, and the current magneto-ARPES data cannot resolve whether a vertical mirror plane is retained or not in the presence of a field. As discussed in Methods and in Extended Data Figs. 6 and 7, this could be due to the weak character of the zero-field C_6 symmetry breaking or, more probably, to domain averaging within the beam spot of the ARPES measurement. As our samples are glued down, they are not free from residual strain. Considering that our beam spot is much larger than the congruent flux order domains, in the absence of field, the time-reversed pairs of loop-current domains would both appear, averaging out in our ARPES signal. With the application of a field and also in the presence of residual strain, one type of time-reversed loop-current domain would dominate, thus revealing the observed electronic response. To distinguish these scenarios from the one where C_6 symmetry is preserved at zero field, future nano-focused synchrotron-based magneto-ARPES measurements will be helpful.

Regardless of its microscopic origin, the piezomagnetic response, which implies that the CDW state spontaneously breaks TRS, is robust and strongly manifested in the V *d* bands that give rise to the VHS, which are often associated with the emergence of unconventional correlated states in the kagome lattice[8]. A field-induced breaking of the C_6 symmetry is also manifested in the bands made up of the Sb *p* orbitals, which have been proposed to be essential for superconductivity[56]. Our measurements of the ellipticity of this Fermi pocket around the BZ centre, however, do not exhibit a clear sign change when the magnetic field is reversed (Extended Data Fig. 8), in contrast to the clear odd-in-field behaviour displayed by the anisotropy of the V *d* bands.

Interestingly, the field response of the V 3*d* bands vanishes at T_{CDW}, whereas that of the Sb p_z bands persists above T_{CDW}. The origin of the latter behaviour and its connection to the CDW order will require further study. Interestingly, a recent magneto-torque measurement reported rotational symmetry breaking above T_{CDW}, which was interpreted as the breaking of inversion symmetry[46] but is not the case in our magneto-ARPES data. One possibility is that strong fluctuations persist above T_{CDW} and are, thus, 'picked up' by the magnetic field, like how a small residual strain induces robust nematic order in iron-based superconductors due to the enlarged nematic susceptibility[57]. Indeed, it has been demonstrated that CsV_3Sb_5 is extremely sensitive to both magnetic field and strain[33], and our glued sample is not free from random residual strain, which may combine with the external magnetic field to induce an ordered state. Alternatively, the magnetic field could also enhance the separation between the onsets of the CDW and loop-current order parameters in certain loop-current configurations[24–26]. In either scenario, however, it is puzzling why this behaviour is seen only in the Sb bands and why the anisotropy is larger outside the CDW phase than inside the CDW phase. It remains to be seen whether future experiments can map the electronic response of the distinct momentum-space regions to decoupled strain and magnetic fields, which will be helpful in disentangling the different microscopic mechanisms. The new capability of magneto-ARPES demonstrated here, which enables the mapping of the spectral response in a momentum-resolved way in the presence of a tunable finite magnetic field, opens up that possibility.

Online content

Any methods, additional references, Nature Portfolio reporting summaries, source data, extended data, supplementary information, acknowledgements, peer review information; details of author contributions and competing interests; and statements of data and code availability are available at https://doi.org/10.1038/s41567-026-03205-7.

References

1. Syozi, I. Statistics of kagome lattice. *Prog. Theor. Phys.* **6**, 306–308 (1951).
2. Balents, L. Spin liquids in frustrated magnets. *Nature* **464**, 199–208 (2010).
3. Han, T.-H. et al. Fractionalized excitations in the spin-liquid state of a kagome-lattice antiferromagnet. *Nature* **492**, 406–410 (2012).
4. Mielke, A. Ferromagnetism in the Hubbard model on line graphs and further considerations. *J. Phys. A* **24**, 3311–3321 (1991).
5. Tanaka, A. & Ueda, H. Stability of ferromagnetism in the Hubbard model on the kagome lattice. *Phys. Rev. Lett.* **90**, 067204 (2003).
6. Yu, S.-L. & Li, J.-X. Chiral superconducting phase and chiral spin-density-wave phase in a Hubbard model on the kagome lattice. *Phys. Rev. B* **85**, 144402 (2012).
7. Kiesel, M. L. & Thomale, R. Sublattice interference in the kagome Hubbard model. *Phys. Rev. B* **86**, 121105 (2012).
8. Kiesel, M. L., Platt, C. & Thomale, R. Unconventional Fermi surface instabilities in the kagome Hubbard model. *Phys. Rev. Lett.* **110**, 126405 (2013).

9. Norman, M. R. Colloquium: Herbertsmithite and the search for the quantum spin liquid. *Rev. Mod. Phys.* **88**, 041002 (2016).
10. Ko, W.-H., Lee, P. A. & Wen, X.-G. Doped kagome system as exotic superconductor. *Phys. Rev. B* **79**, 214502 (2009).
11. Wang, W.-S., Li, Z.-Z., Xiang, Y.-Y. & Wang, Q.-H. Competing electronic orders on kagome lattices at Van Hove filling. *Phys. Rev. B* **87**, 115135 (2013).
12. Liu, T. Strain-induced pseudomagnetic field and quantum oscillations in kagome crystals. *Phys. Rev. B* **102**, 045151 (2020).
13. Wang, J. et al. Controlled frustration release on the kagome lattice by uniaxial-strain tuning. *Phys. Rev. Lett.* **131**, 256501 (2023).
14. Lima, W. P., da Costa, D. R., Sena, S. H. R. & Pereira, J. M. Effects of uniaxial and shear strains on the electronic spectrum of Lieb and kagome lattices. *Phys. Rev. B* **108**, 125433 (2023).
15. Dey, M., Maiti, S. K. & Karmakar, S. N. Magnetic field induced metal-insulator transition in a kagome nanoribbon. *J. Appl. Phys.* **110**, 094306 (2011).
16. Kang, M. et al. Dirac fermions and flat bands in the ideal kagome metal FeSn. *Nat. Mater.* **19**, 163–169 (2020).
17. Ortiz, B. R. et al. New kagome prototype materials: discovery of KV_3Sb_5, RbV_3Sb_5, and CsV_3Sb_5. *Phys. Rev. Mater.* **3**, 094407 (2019).
18. Ortiz, B. R. et al. CsV_3Sb_5: a Z_2 topological kagome metal with a superconducting ground state. *Phys. Rev. Lett.* **125**, 247002 (2020).
19. Tan, H., Liu, Y., Wang, Z. & Yan, B. Charge density waves and electronic properties of superconducting kagome metals. *Phys. Rev. Lett.* **127**, 046401 (2021).
20. Christensen, M. H., Birol, T., Andersen, B. M. & Fernandes, R. M. Theory of the charge density wave in AV_3Sb_5 kagome metals. *Phys. Rev. B* **104**, 214513 (2021).
21. Park, T., Ye, M. & Balents, L. Electronic instabilities of kagome metals: saddle points and Landau theory. *Phys. Rev. B* **104**, 035142 (2021).
22. Lin, Y.-P. & Nandkishore, R. M. Complex charge density waves at Van Hove singularity on hexagonal lattices: Haldane-model phase diagram and potential realization in the kagome metals AV_3Sb_5 (A=K, Rb, Cs). *Phys. Rev. B* **104**, 045122 (2021).
23. Denner, M. M., Thomale, R. & Neupert, T. Analysis of charge order in the kagome metal AV_3Sb_5 (A = K, Rb, Cs). *Phys. Rev. Lett.* **127**, 217601 (2021).
24. Christensen, M. H., Birol, T., Andersen, B. M. & Fernandes, R. M. Loop currents in AV_3Sb_5 kagome metals: multipolar and toroidal magnetic orders. *Phys. Rev. B* **106**, 144504 (2022).
25. Wagner, G., Guo, C., Moll, P. J. W., Neupert, T. & Fischer, M. H. Phenomenology of bond and flux orders in kagome metals. *Phys. Rev. B* **108**, 125136 (2023).
26. Tazai, R., Yamakawa, Y. & Kontani, H. Drastic magnetic-field-induced chiral current order and emergent current-bond-field interplay in kagome metals. *Proc. Natl Acad. Sci. USA* **121**, e2303476121 (2024).
27. Mielke, C. et al. Time-reversal symmetry-breaking charge order in a kagome superconductor. *Nature* **602**, 245–250 (2022).
28. Khasanov, R. et al. Time-reversal symmetry broken by charge order in CsV_3Sb_5. *Phys. Rev. Res.* **4**, 023244 (2022).
29. Jiang, Y.-X. et al. Unconventional chiral charge order in kagome superconductor KV_3Sb_5. *Nat. Mater.* **20**, 1353–1357 (2021).
30. Xing, Y. et al. Optical manipulation of the charge-density-wave state in RbV_3Sb_5. *Nature* **631**, 60–66 (2024).
31. Guo, C. et al. Switchable chiral transport in charge-ordered kagome metal CsV_3Sb_5. *Nature* **611**, 461–466 (2022).
32. Wei, X. et al. Three-dimensional hidden phase probed by in-plane magnetotransport in kagome metal CsV_3Sb_5 thin flakes. *Nat. Commun.* **15**, 5038 (2024).
33. Guo, C. et al. Correlated order at the tipping point in the kagome metal CsV_3Sb_5. *Nat. Phys.* **20**, 579–584 (2024).
34. Xu, Y. et al. Three-state nematicity and magneto-optical Kerr effect in the charge density waves in kagome superconductors. *Nat. Phys.* **18**, 1470–1475 (2022).
35. Farhang, C., Wang, J., Ortiz, B. R., Wilson, S. D. & Xia, J. Unconventional specular optical rotation in the charge ordered state of kagome metal CsV_3Sb_5. *Nat. Commun.* **14**, 5326 (2023).
36. Saykin, D. R. et al. High resolution polar Kerr effect studies of CsV_3Sb_5: tests for time-reversal symmetry breaking below the charge-order transition. *Phys. Rev. Lett.* **131**, 016901 (2023).
37. Wang, J., Farhang, C., Ortiz, B. R., Wilson, S. D. & Xia, J. Resolving the discrepancy between MOKE measurements at 1550-nm wavelength on kagome metal CsV_3Sb_5. *Phys. Rev. Mater.* **8**, 014202 (2024).
38. Nie, L. et al. Charge-density-wave-driven electronic nematicity in a kagome superconductor. *Nature* **604**, 59–64 (2022).
39. Xiang, Y. et al. Twofold symmetry of c-axis resistivity in topological kagome superconductor CsV_3Sb_5 with in-plane rotating magnetic field. *Nat. Commun.* **12**, 6727 (2021).
40. Jin, F. et al. π phase interlayer shift and stacking fault in the kagome superconductor CsV_3Sb_5. *Phys. Rev. Lett.* **132**, 066501 (2024).
41. Liu, Z. et al. Absence of E_{2g} nematic instability and dominant A_{1g} response in the kagome metal CsV_3Sb_5. *Phys. Rev. X* **14**, 031015 (2024).
42. Wulferding, D. et al. Emergent nematicity and intrinsic versus extrinsic electronic scattering processes in the kagome metal CsV_3Sb_5. *Phys. Rev. Res.* **4**, 023215 (2022).
43. Zhao, H. et al. Cascade of correlated electron states in the kagome superconductor CsV_3Sb_5. *Nature* **599**, 216–221 (2021).
44. Chen, H. et al. Roton pair density wave in a strong-coupling kagome superconductor. *Nature* **599**, 222–228 (2021).
45. Li, H. et al. Rotation symmetry breaking in the normal state of a kagome superconductor KV_3Sb_5. *Nat. Phys.* **18**, 265–270 (2022).
46. Asaba, T. et al. Evidence for an odd-parity nematic phase above the charge-density-wave transition in a kagome metal. *Nat. Phys.* **20**, 40–46 (2024).
47. Huang, J. et al. Angle-resolved photoemission spectroscopy with an in situ tunable magnetic field. *Rev. Sci. Instrum.* **94**, 093902 (2023).
48. Damascelli, A., Hussain, Z. & Shen, Z.-X. Angle-resolved photoemission studies of the cuprate superconductors. *Rev. Mod. Phys.* **75**, 473–541 (2003).
49. Sobota, J. A., He, Y. & Shen, Z.-X. Angle-resolved photoemission studies of quantum materials. *Rev. Mod. Phys.* **93**, 025006 (2021).
50. Liu, Z. et al. Charge-density-wave-induced bands renormalization and energy gaps in a kagome superconductor RbV_3Sb_5. *Phys. Rev. X* **11**, 041010 (2021).
51. Luo, H. et al. Electronic nature of charge density wave and electron-phonon coupling in kagome superconductor KV_3Sb_5. *Nat. Commun.* **13**, 273 (2022).
52. Kang, M. et al. Twofold Van Hove singularity and origin of charge order in topological kagome superconductor CsV_3Sb_5. *Nat. Phys.* **18**, 301–308 (2022).
53. Hu, Y. et al. Rich nature of Van Hove singularities in kagome superconductor CsV_3Sb_5. *Nat. Commun.* **13**, 2220 (2022).
54. Ryu, S. H. et al. magnetoARPES: angle resolved photoemission spectroscopy with magnetic field control. *J. Electron Spectrosc. Relat. Phenom.* **266**, 147357 (2023).
55. Ebert, H., Ködderitzsch, D. & Minár, J. Calculating condensed matter properties using the KKR-Green's function method—recent developments and applications. *Rep. Prog. Phys.* **74**, 096501 (2011).
56. Ritz, E. T. et al. Superconductivity from orbital-selective electron-phonon coupling in AV_3Sb_5. *Phys. Rev. B* **108**, L100510 (2023).
57. Fernandes, R. M., Chubukov, A. V. & Schmalian, J. What drives nematic order in iron-based superconductors? *Nat. Phys.* **10**, 97–104 (2014).

[1]Department of Physics and Astronomy, Rice University, Houston, TX, USA. [2]Smalley-Curl Institute, Rice University, Houston, TX, USA. [3]Department of Condensed Matter Physics, Weizmann Institute of Science, Rehovot, Israel. [4]Applied Physics Graduate Program, Smalley-Curl Institute, Rice University, Houston, TX, USA. [5]Department of Physics, University of Washington, Seattle, WA, USA. [6]Department of Electrical and Computer Engineering, Rice University, Houston, TX, USA. [7]Department of Materials Science and NanoEngineering, Rice University, Houston, TX, USA. [8]Rice Laboratory for Emergent Magnetic Materials, Rice University, Houston, TX, USA. [9]Department of Applied Physics, Yale University, New Haven, CT, USA. [10]New Technologies - Research Centre, University of West Bohemia in Pilsen, Plzeň, Czech Republic. [11]Department of Physics, Boston College, Chestnut Hill, MA, USA. [12]Department of Physics, The Pennsylvania State University, University Park, PA, USA. [13]Department of Physics, The Grainger College of Engineering, University of Illinois Urbana-Champaign, Urbana, IL, USA. [14]Anthony J. Leggett Institute for Condensed Matter Theory, University of Illinois Urbana-Champaign, Urbana, IL, USA. [15]These authors contributed equally: Jianwei Huang, Zheng Ren. ✉e-mail: jwhuang0rice@gmail.com; mingyi@rice.edu

Methods

Sample growth and characterization

Single crystals of CsV_3Sb_5 were grown with the self-flux method described in ref. 58 and ref. 41. The crystal sizes were 3 mm × 3 mm with a typical residual resistivity ratio up to ~120. The resistivity measurements were performed in DynaCool (Quantum Design) with lock-in amplifiers and voltage preamplifiers (SR860, Stanford Research).

Magneto-ARPES measurements

The ARPES experiments were performed using a laboratory system equipped with a helium lamp that produced light with 75% linear vertical polarization and 25% linear horizontal polarization and an electron analyser (DA30, Scienta). The angular resolution was set to 0.3°. The total energy resolution was set to 13 meV. All samples were cleaved in situ at around 30 K, and all measurements were made in an ultrahigh vacuum with a base pressure lower than 1×10^{-10} Torr. We reproduced the results with several samples.

An in situ magnetic field was applied using a magnetic coil mounted around the sample on the sample stage[47] (Fig. 1e,f). Samples were placed at the centre of the magnetic coil flush with the top surface of the coil so that the magnetic field was oriented along the out-of-plane direction at the sample position. The magnitude of the field was controlled by adjusting the electric current flowing through the magnetic coil, which was characterized outside the ultrahigh vacuum before the experiments[47]. The magnetic field direction could be reversed by reversing the direction of the electric current. In this experimental set-up, the primary extrinsic effects of the magnetic field on the ARPES measurements were the rotation of the constant-energy contour, contraction of the photoelectron emission angle and momentum broadening[47]. In this study, with the small applied magnetic field, only a rigid rotation of the constant-energy contour was observed, which could be corrected post-measurements. All the ARPES measurements were performed using the DA30 deflector mode unless otherwise noted.

DFT calculations

The DFT first-principles calculations were performed with the Vienna Ab Initio Simulation Package[59]. The generalized gradient approximation parameterized by Perdew, Burke and Ernzerhof[60] was employed for the exchange-correlation interaction between electrons throughout. The cutoff energy of the plane-wave basis set was 300 eV. The pristine phase of CsV_3Sb_5 was used to calculate the electronic structures. Notice that the crystal structure was obtained from ref. 19. Spin–orbit coupling was not involved in the structural relaxation but was considered in the calculations of the band structure. A k-mesh of 12 × 12 × 6 was used to sample the BZ.

Simulation of magneto-dichroism of ARPES spectra

We observed magneto-dichroism in the ARPES spectra between the two adjacent K regions when applying opposite magnetic fields along the c axis (Fig. 2). We have shown that the magneto-dichroism arises from the selective broadening of the bands at different K regions (Figs. 2 and 3). The effect can be qualitatively simulated with the single-particle spectral function $A(\mathbf{k}, \omega)$ by manually assigning different imaginary components to the self-energy for bands around the two K regions (Extended Data Fig. 3). $A(\mathbf{k}, \omega)$ is described by:

$$A(\mathbf{k},\omega) = -\frac{1}{\pi}\frac{\Sigma''(\mathbf{k},\omega)}{[\omega - \epsilon_{\mathbf{k}} - \Sigma'(\mathbf{k},\omega)]^2 + [\Sigma''(\mathbf{k},\omega)]^2}, \quad (1)$$

$\epsilon_{\mathbf{k}}$ is the bare band dispersion and taken from the DFT calculations (dashed lines in Extended Data Fig. 3). $\Sigma'(\mathbf{k},\omega)$ is the real part of the self energy. $\Sigma''(\mathbf{k}, \omega)$ is the imaginary part of the self energy and obtained by fitting the linewidth of the corresponding experimental data. A momentum- and energy-independent $\Sigma''(\mathbf{k}, \omega)$ was adopted for the simulation. The entire spectrum is then multiplied by a Fermi distribution at 25 K. On applying a positive magnetic field, $\Sigma''(\mathbf{k}, \omega)$ values of 0.21 eV and 0.15 eV were individually used for $A(\mathbf{k}, \omega)$, corresponding to the simulated ARPES spectra around different K regions (left-hand and right-hand parts of Extended Data Fig. 3a,d). When the magnetic field was reversed, the opposite $\Sigma''(\mathbf{k}, \omega)$ values were used. The simulated spectra exhibit similar magneto-dichroism to that observed in the experimental data (Extended Data Fig. 1).

One-step model ARPES calculations

To understand the matrix-element effects in the ARPES experiments under external magnetic fields, we carried out ab initio one-step model ARPES calculations using the spin-polarized relativistic Korringa–Kohn–Rostoker package[55] under the fully relativistic four-component Dirac formalism and the atomic-sphere approximation. The chosen exchange-correlation functional is based on the local spin density approximation by Vosko, Wilk and Nusair[61]. An angular momentum cutoff of $l = 3$ was adopted for solving the Korringa–Kohn–Rostoker equations. During the self-consistent field calculations, the BZ integration was carried out on an equidistant 29 × 29 × 14 k-mesh and the energy integral was evaluated for 32 points along the Gaussian–Legendre quadrature path. For each external magnetic field, the self-consistent field calculations were converged separately. Lloyd's formula was employed to determine the Fermi level. The one-step ARPES calculations considered a semi-infinite surface model terminated by the Sb atoms. The next layer was the V–Sb slab rather than Cs atoms. The surface barrier was of the z-dependent Rundgren–Malmström type[62]. The experimental light incidence angles and the photon energy of 21.2 eV were adopted in the calculations. To simulate the mixed polarization of the helium lamp, the final calculated one-step ARPES spectra were obtained through a linear superposition of 25% p-polarization and 75% s-polarization results. The effects of the lifetimes of the initial and final states were simulated by imaginary potentials of 0.05 eV and 1.5 eV, respectively. The external magnetic field theoretically enters all three parts of the photoemission matrix elements: initial states, the relativistic dipole operator and the spin-polarized time-reversed low-energy electron diffraction final states, the treatment of which has been described previously for ferromagnetic materials[63]. The classical photoelectron deflection in the vacuum due to the Lorentz force under magnetic fields was not considered in the one-step model ARPES calculations.

The results of the calculations are summarized in Extended Data Fig. 5. First, we show the zero-field constant-energy contour 260 meV below the Fermi level (Extended Data Fig. 5a). Notice that the Fermi level in the calculations is ~90 meV higher than the one in experiments. Therefore, the theoretical constant-energy contour in Extended Data Fig. 5a has a reasonable resemblance to the experimental $E - E_F = -0.35$ eV constant-energy contour of Fig. 2a taken slightly below the Dirac cone. Without adjusting the theoretical Fermi level, we extracted the momentum slice cut 1 at $k_x = 0.5$ Å^{-1} and compared its band dispersions and MDCs under large external fields of opposite directions around 117.5 T. The results are summarized in Extended Data Fig. 5b–d. The horizontal dashed lines near the inner peaks of the MDC (taken at $E - E_F = -0.2$ eV) clearly indicate a left–right symmetric feature at 0 T but field-odd asymmetric behaviour under the large magnetic fields applied. Although this may seem consistent with the experimental data in Fig. 2e–g, the fields required to observe this asymmetry in the simulations are five orders of magnitude larger than the experimental ones. The difference in the theoretical calculations here is that the TRS breaking comes from the large magnetic fields and the induced moments on the V atoms, which were treated within the DFT. To gain further insights on the asymmetric MDC peaks in Extended Data Fig. 5c,d, we present the spin-resolved MDCs under different magnetic fields in Extended Data Fig. 5e–g with the projection axis along z. If we were to consider only the out-of-plane magnetic field, which breaks the TRS and all vertical mirrors, the magnetic mirror M_xT (containing Γ–K) would persist, which would protect the band degeneracy between $E(k_x, k_y)$ and

$E(k_x, -k_y)$. Therefore, we infer that spin-dependent multiple scattering and relativistic effects could contribute to the asymmetric MDC line shapes with respect to the Γ–M plane. However, this becomes discernible in the calculations only with magnetic fields nearly five orders of magnitude larger than the experimental ones. As a comparison, we show in Extended Data Fig. 5h the spin-integrated MDCs for cut 1 taken at $E - E_F = -0.2$ eV under fields of 0 T, +2.35 T and −2.35 T. The calculated results clearly overlap with each other without any signatures of the magneto-dichroism observed in the ARPES experiments.

Model for the fingerprints of piezomagnetism in ARPES

We adopted a phenomenological model to shed light on the manifestations of piezomagnetism in our magneto-ARPES data. Specifically, we considered the congruent CDW flux phase proposed in ref. 30, which has the non-zero piezomagnetic tensor component Λ_{xyz}, defined as $\varepsilon_{ij} = \Lambda_{ijk} B_k$, where ε_{ij} is the strain tensor and B_k is the magnetic field. Thus, Λ_{xyz} implies that a non-zero shear strain ε_{xy} is induced by an out-of-plane field B_z. Importantly, the congruent CDW flux phase also displays a non-zero distortion $\varepsilon_{xx} - \varepsilon_{xy}$ in the absence of a magnetic field. Our goal is to model the impact of both effects on the V and Sb Fermi surfaces.

We start with the large kagome Fermi surface for vanadium. For simplicity, we model it in terms of a simple tight-binding model on the kagome lattice. Denoting the three kagome sublattices as A, B and C, and following the coordinate system of ref. 64, the nearest-neighbour tight-binding model is given by:

$$\mathcal{H}_0 = \sum_{\mathbf{k},\sigma} \Psi^{\dagger}_{\mathbf{k}\sigma} H_0(\mathbf{k}) \Psi_{\mathbf{k}\sigma}, \tag{2}$$

where $\Psi_{\mathbf{k}\sigma} = (\psi_{A,\mathbf{k}\sigma}, \psi_{B,\mathbf{k}\sigma}, \psi_{C,\mathbf{k}\sigma})^{\mathrm{T}}$, and

$$H_0(\mathbf{k}) = -2t \begin{pmatrix} 0 & \cos k_1 & \cos k_2 \\ \cos k_1 & 0 & \cos k_3 \\ \cos k_2 & \cos k_3 & 0 \end{pmatrix} - \mu \begin{pmatrix} 1 & 0 & 0 \\ 0 & 1 & 0 \\ 0 & 0 & 1 \end{pmatrix}. \tag{3}$$

Here μ denotes the chemical potential, t is the hopping parameter and $k_1 = k_x$, $k_2 = \frac{k_x}{2} + \frac{\sqrt{3}k_y}{2}$ and $k_3 = -\frac{k_x}{2} + \frac{\sqrt{3}k_y}{2}$. The band structure has a saddle point at $\mu = 0$, resulting in a perfectly hexagonal Fermi surface.

In the congruent CDW flux phase proposed in ref. 30, two more terms emerge:

$$\mathcal{H} = \mathcal{H}_0 + \mathcal{H}_1, \tag{4}$$

with

$$H_1(\mathbf{k}) = \frac{\Phi_1}{\sqrt{3}} \begin{pmatrix} 1 & 0 & 0 \\ 0 & 1 & 0 \\ 0 & 0 & -2 \end{pmatrix} + \Phi_2 B_z \begin{pmatrix} 1 & 0 & 0 \\ 0 & -1 & 0 \\ 0 & 0 & 0 \end{pmatrix}. \tag{5}$$

Here Φ_1 and Φ_2 are parameters that transform as the $d_{x^2-y^2}$ and d_{xy} form factors, respectively, and B_z is the out-of-plane magnetic field. Note that this parameterization gives one of the domains only. Although both terms individually break C_6 symmetry, their combination also breaks all in-plane twofold rotation axes (all vertical mirrors). We can diagonalize $H_0(\mathbf{k}) + H_1(\mathbf{k})$ to obtain the distorted Fermi surface under a magnetic field. We note that because the congruent CDW flux phase breaks translational symmetry, it also folds the band structure. We did not include these effects, as we focused on the piezomagnetic effect.

That the ARPES data without a magnetic field is C_6 symmetric indicates that either $\Phi_1 = 0$ or $\Phi_1 \ll t$, as shown in Extended Data Fig. 6. For the calculations incorporating a non-zero magnetic field, we adopted $\Phi_1 = 0.01t$.

To visualize the behaviour of the Fermi surface in the presence of a magnetic field with this model, we set $\mu = 0.16t$ (to be slightly away from perfect nesting) and calculated the Fermi surface with the parameters $(t, \Phi_1, \Phi_2 B_z) = (1, 0.01, 0.1)$ to represent a positive magnetic field and $(t, \Phi_1, \Phi_2 B_z) = (1, 0.01, -0.1)$ to represent a negative magnetic field (Extended Data Fig. 7). The Fermi surfaces obtained in the presence of a magnetic field for both situations preserve inversion symmetry but break the mirror symmetry with respect to the horizontal Γ–M plane (Extended Data Fig. 7b,c). This is consistent with the C_6 symmetry breaking observed in the experimental data, which, however, is manifested in the spectral weight distribution of the Fermi surface.

For the small Sb Fermi pocket, it suffices to model the electronic dispersion in terms of a parabolic dispersion with two broken-symmetry terms analogous to Φ_1 and Φ_2 in equation (5):

$$E(k, \theta) = \left(\frac{k^2}{2m} - \tilde{\mu}\right) + \tilde{\Phi}_1 k^2 \cos(2\theta) + \tilde{\Phi}_2 B_z k^2 \sin(2\theta), \tag{6}$$

where θ is the angle with respect to the k_x axis, which corresponds to the Γ–M direction, m is the effective mass of the electron and the tildes are used to distinguish the Φ_1 and Φ_2 parameters here from those used for the large Fermi pocket. We use this equation to fit the angle dependence of the diameter of the Fermi surface extracted from the ARPES data. To simplify the notation, we rewrite the equation above as follows:

$$E(k, \theta) = (A_1 k^2 - \mu) + A_2 k^2 \cos(2\theta) + A_3 k^2 \sin(2\theta) \tag{7}$$

To accurately capture the distortion of the Fermi surface under a magnetic field, we first extracted the diameter of the Fermi surface as a function of the Fermi surface angle by fitting the Fermi surface mappings obtained with and without a magnetic field (Extended Data Fig. 8a). We then normalized the diameter of the Fermi surface under a magnetic field by dividing it by the diameter measured without a magnetic field, thus excluding potential extrinsic effects. The normalized diameter of the Fermi surface as a function of the Fermi surface angle exhibits a more pronounced twofold rotational symmetry (Fig. 4j). We then fitted the Fermi momentum using equation (7) (Extended Data Fig. 8b), yielding fitting parameters $A_2/A_1 \approx 0.050$ and $A_3/A_1 \approx 0.011$. The fitting results reveal a consistent angular deviation of the longitudinal axis of the elliptical Fermi surface from the BZ high-symmetry direction, in agreement with the fitting approach used in the main text.

Data availability

All data needed to evaluate the conclusions are available from the corresponding authors upon reasonable request. Source data are provided with this paper.

Code availability

The band structure calculations used in this study are available from the corresponding authors upon reasonable request.

References

58. Qian, T. et al. Revealing the competition between charge density wave and superconductivity in CsV_3Sb_5 through uniaxial strain. *Phys. Rev. B* **104**, 144506 (2021).
59. Kresse, G. & Furthmüller, J. Efficient iterative schemes for ab initio total-energy calculations using a plane-wave basis set. *Phys. Rev. B* **54**, 11169–11186 (1996).
60. Perdew, J. P., Burke, K. & Ernzerhof, M. Generalized gradient approximation made simple. *Phys. Rev. Lett.* **77**, 3865 (1996); erratum **78**, 1396 (1997).
61. Vosko, S. H., Wilk, L. & Nusair, M. Accurate spin-dependent electron liquid correlation energies for local spin density calculations: a critical analysis. *Can. J. Phys.* **58**, 1200–1211 (1980).

62. Rundgren, J. & Malmstrom, J. Transmission and reflection of low-energy electrons at the surface barrier of a metal. *J. Phys. C* **10**, 4671 (1977).
63. Braun, J. The theory of angle-resolved ultraviolet photoemission and its applications to ordered materials. *Rep. Prog. Phys.* **59**, 1267 (1996).
64. Guo, H.-M. & Franz, M. Topological insulator on the kagome lattice. *Phys. Rev. B* **80**, 113102 (2009).

Acknowledgements

The ARPES work at Rice University was supported by the Gordon and Betty Moore Foundation's EPiQS Initiative (Grant No. GBMF9470 to M.Y.), the Robert A. Welch Foundation (Grant No. C-2175 to M.Y.) and the US Department of Energy, Basic Energy Sciences (Grant Nos. DE-SC0021421 to M.Y. and DE-SC0026179). The single-crystal synthesis work at UW was supported by the Air Force Office of Scientific Research (Award No. FA2386-21-1-4060 to J.-H.C.) and the David Lucile Packard Foundation (J.-H.C.). R.M.F. was supported by the Air Force Office of Scientific Research (Award No. FA9550-21-1-0423). Z.W. is supported by the US Department of Energy, Basic Energy Sciences (Grant No. DE-FG02-99ER45747). B.Y. acknowledges financial support from the Israel Science Foundation (Grant No. 2974/23) and the National Science Foundation through the Penn State Materials Research Science and Engineering Center (Grant No. DMR 2011839). Efforts to grow single crystals at Rice are supported by the US Department of Energy, Basic Energy Sciences (Grant No. DE-SC0026179 to P.D.). Part of the materials characterization efforts at Rice is supported by the Robert A. Welch Foundation (Grant No. C-1839 to P.D.). J.K. acknowledges support from the Robert A. Welch Foundation (Grant No. C-1509) and the Gordon and Betty Moore Foundation (Grant No. 11520). J.M. and A.P. thank the project Quantum Materials for Applications in Sustainable Technologies (QM4ST), funded as Project No. CZ.02.01.01/00/22_008/0004572 by Programme Johannes Amos Comenius, through the Excellent Research call. Y.H. is supported by the Air Force Office of Scientific Research (Award No. FA9550-24-1-0048).

Author contributions

M.Y. and J. Huang proposed and designed the project. Z.L. grew the CsV_3Sb_5 single crystals with the help of J.M.D. under the guidance of J.-H.C. J. Huang, Z.R., J. Hyun, T.A.H. and Z.Y. carried out the ARPES measurements under the guidance of M.Y., Y.H. and J.K. J. Huang performed the magneto-ARPES data analysis. Y.X., Z.L. and J.M.D. grew single crystals for control measurements under the guidance of P.D. and J.-H.C. H.T., B.Y. and Z.W. conducted the first-principles calculations. Y.Z. carried out the ab initio one-step model ARPES calculations with advice from A.P. and J.M. Y.Z. analysed the one-step calculated data. R.M.F. performed the phenomenological theoretical analysis. J. Huang and M.Y. wrote the paper with input from all co-authors.

Competing interests

The authors declare no competing interests.

Additional information

Extended data is available for this paper at https://doi.org/10.1038/s41567-026-03205-7.

Supplementary information The online version contains supplementary material available at https://doi.org/10.1038/s41567-026-03205-7.

Correspondence and requests for materials should be addressed to Jianwei Huang or Ming Yi.

Peer review information *Nature Physics* thanks the anonymous reviewers for their contribution to the peer review of this work.

https://doi.org/10.1038/s41567-026-03205-7

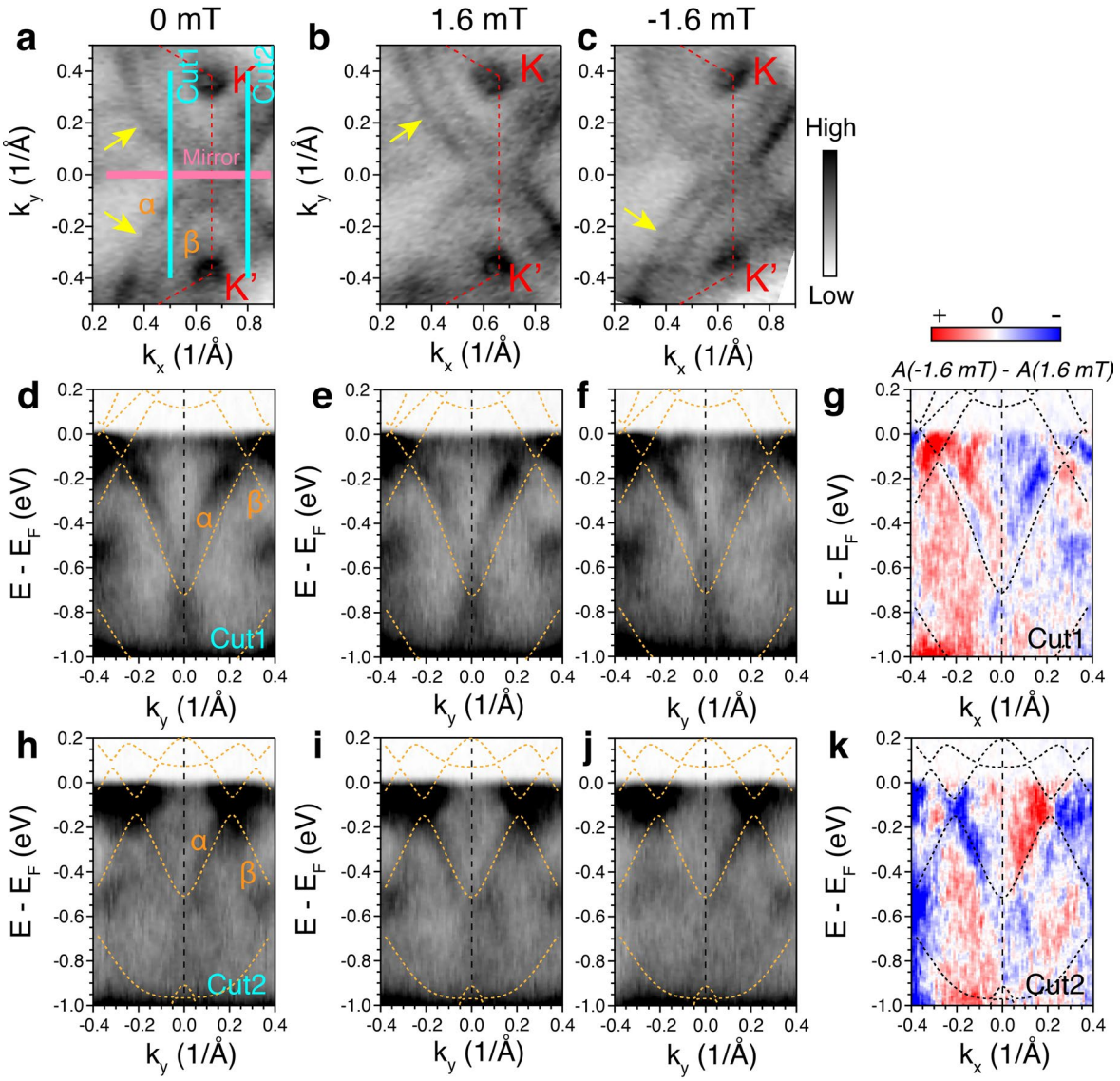

Extended Data Fig. 1 | Electronic response of CsV_3Sb_5 around the K point under a magnetic field. (**a**)-(**c**) Constant energy contours at -0.35 eV without a magnetic field, with +1.6 mT, and with -1.6 mT, respectively. (**d**)-(**e**) The corresponding spectral images along cut1 indicated in (**a**). (**g**) The spectral image obtained by subtracting (**e**) from (**f**). (**h**)-(**k**) Same as (**d**)-(**g**) but along cut2 indicated in (**a**).

https://doi.org/10.1038/s41567-026-03205-7

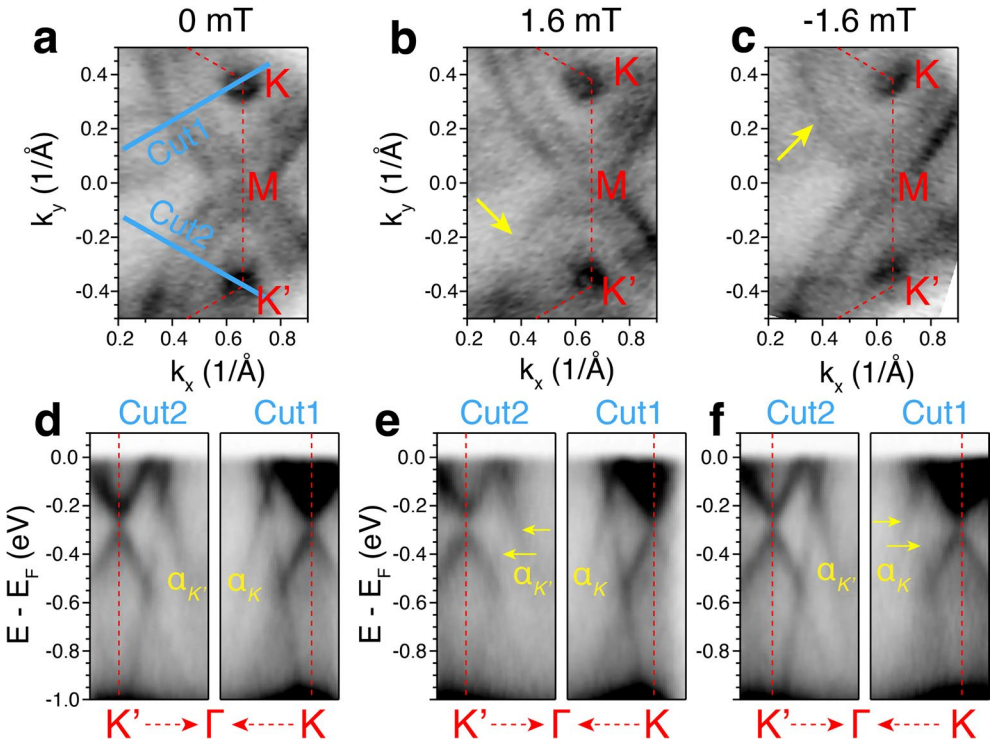

Extended Data Fig. 2 | Momentum-selective spectral broadening in CsV_3Sb_5 under a magnetic field. (**a**)-(**c**) Constant energy contours at -0.35 eV without a magnetic field, with +1.6 mT, and with -1.6 mT, respectively. The yellow arrows point to the Fermi surface sheets that broaden substantially under the corresponding magnetic field. (**d**)-(**f**) Spectral images taken along cut1 and cut2 indicated in (**a**), with cut directions perpendicular to the Fermi surface sheets. Selective momentum broadening of the α and β bands is evident from both the Fermi surface sheets and the corresponding band spectral images.

https://doi.org/10.1038/s41567-026-03205-7

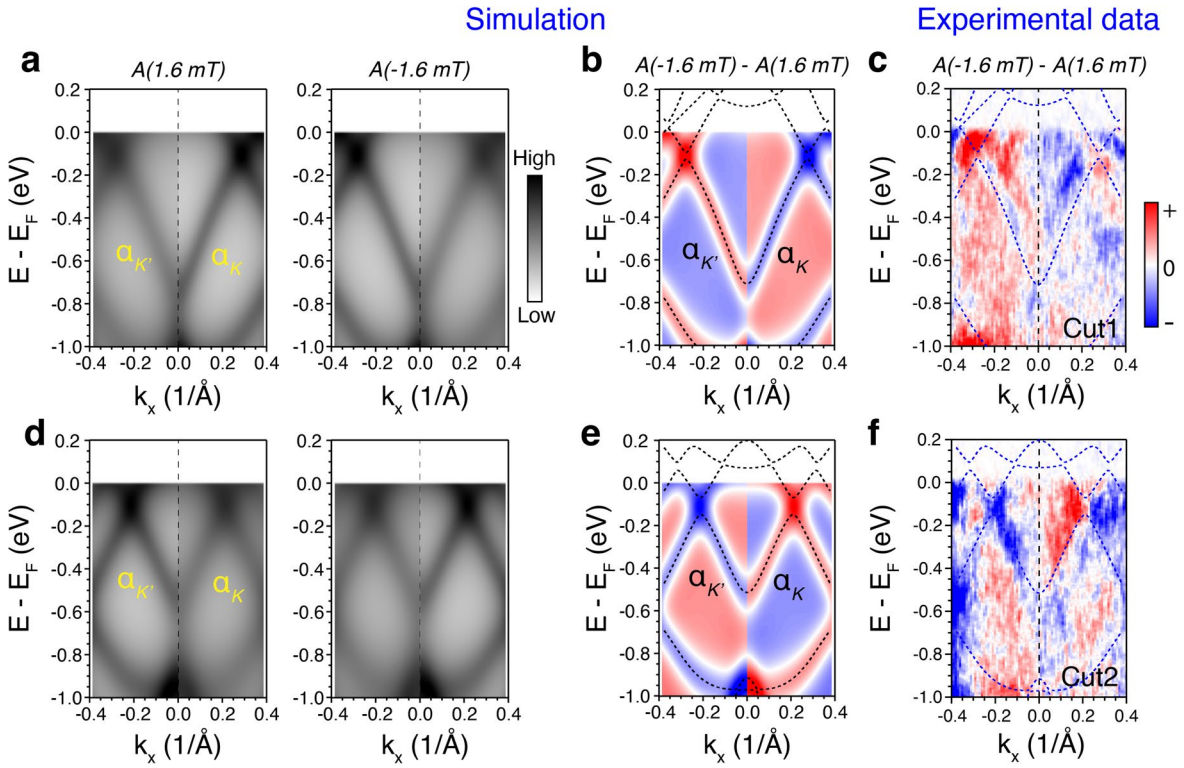

Extended Data Fig. 3 | Simulation of the magneto-dichroic effect of the ARPES spectra. (**a**) Simulated spectral images to reproduce the ARPES observations based on the band structure obtained by DFT calculations (black dashed line in (**c**)). The DFT band dispersions were extracted along the momentum path along cut1 in Fig. 2b of the main text. Distinct imaginary parts of the self-energies were applied to the left and right momentum regions in each panel to simulate the momentum-selective spectral broadening under a magnetic field. (**b**) Simulated magneto-dichroic spectral image by subtracting the left panel from the right panel in (**a**). (**c**) Measured magneto-dichroic spectral image from Fig. 2h in main text. (**d**)-(**f**) Same as (**a**)-(**c**) but simulating the magneto-dichroic spectral image along cut2 in Fig. 2b of the main text.

https://doi.org/10.1038/s41567-026-03205-7

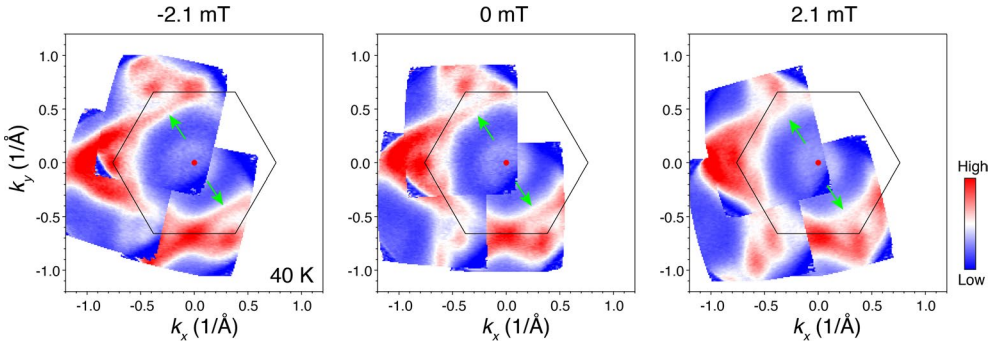

Extended Data Fig. 4 | Constant energy contour mappings showing the two opposite K regions. Constant energy contours at -0.2 eV consist of three separate DA30 deflector mode mappings on the same sample, showing the two opposite K regions using a helium lamp light source. The mappings were taken at magnetic fields of -2.1 mT, 0 mT, and 2.1 mT. The green arrows point to the Fermi surface sheets respond most prominently to the magnetic field. The two Fermi surface sheets around the two opposite K regions exhibit the same behavior, which is also evident by our observations in Fig. 2c,d of the main text considering the crystalline translational symmetry.

https://doi.org/10.1038/s41567-026-03205-7

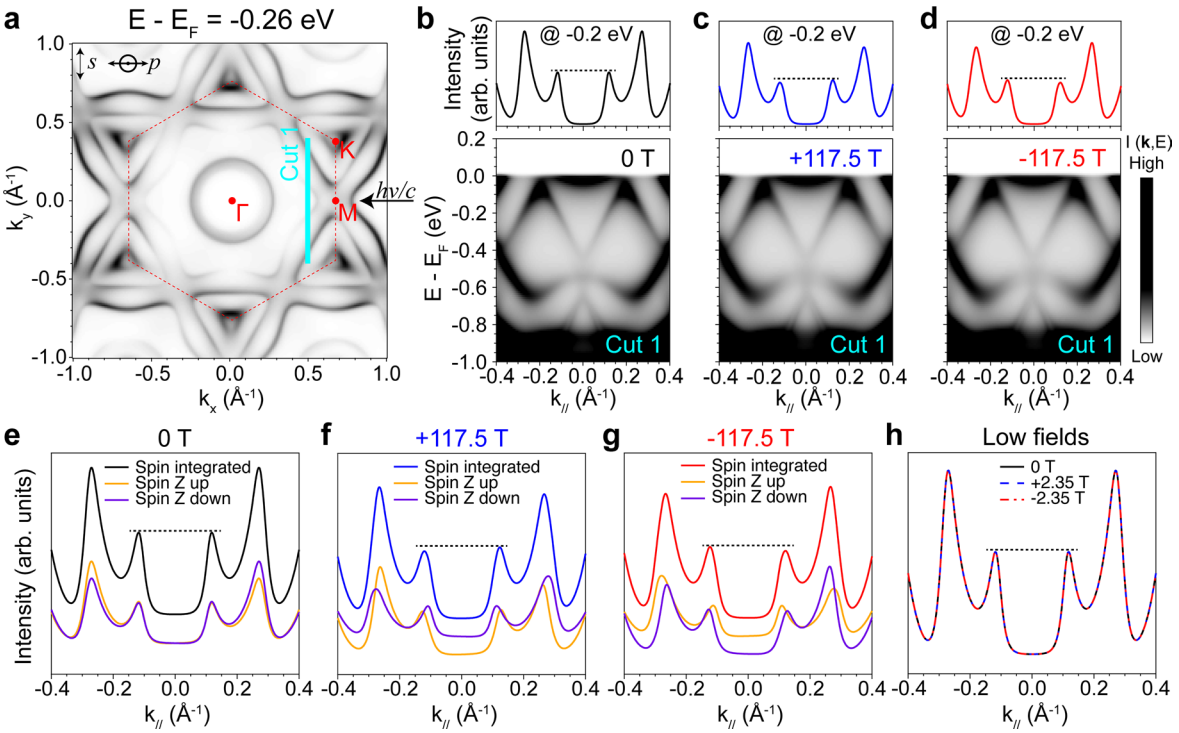

Extended Data Fig. 5 | One-step model ARPES calculations of CsV_3Sb_5 under external magnetic fields within the atomic-sphere approximation. (**a**) Constant energy contour under zero field calculated at E - EF = -0.26 eV using experimental geometry and inputs. Photon incidence direction and the s and p polarizations of photons are illustrated by the hν/c and the symbols on the top left. (**b**) ARPES spectra of Cut 1 spanned by the vertical cyan line in (**a**), similar to experiments performed in main text Fig. 2(e). The momentum distribution curve (MDC) taken at E - EF = -0.2 eV is shown on top. A Fermi-Dirac distribution function of 20 K convolved with a putative 20 meV experimental resolution is applied to the calculated data. (**c**, **d**) Same as (**b**), but under external magnetic fields of +117.5 and -117.5 T, respectively. (**e** - **g**) Spin integrated MDCs reproduced from (b-d) and their spin-resolved components projected along z under 0, +117.5, and -117.5 T, respectively. (**h**) Spin-integrated MDCs taken at E - EF = -0.2 eV of Cut 1 but at low fields of 0, +2.35, and -2.35 T.

https://doi.org/10.1038/s41567-026-03205-7

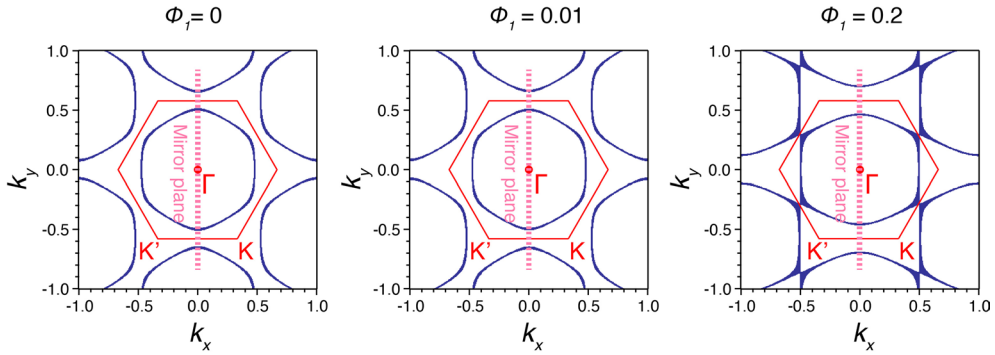

Extended Data Fig. 6 | Fermi surface of the nearest-neighbor kagome model of Methods Section F in the absence of a magnetic field. The parameters are set as t = 1 and μ = -0.08. Bz = 0 to focus on the effect of Φ1, which is varied as indicated in each panel (Φ1 = 0, 0.01, and 0.2). As expected, the Fermi surface distortion is negligible for small Φ1.

https://doi.org/10.1038/s41567-026-03205-7

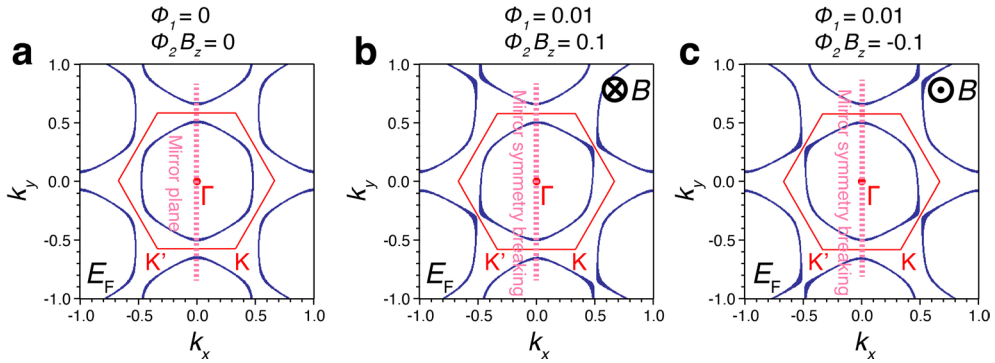

Extended Data Fig. 7 | Fermi surface of the nearest-neighbor kagome model of Methods Section F in the presence of a magnetic field. (**a**) Fermi surface for t = 1, μ = -0.08, Φ1 = 0 and Bz = 0. The horizontal mirror plane is preserved. (**b**) Fermi surface with t = 1 and μ = -0.08, but now with Φ1 = 0.01 and a positive field Φ2Bz = 0.1. (**c**) Same as (**b**) but with a negative field Φ2Bz = -0.1. In both (**b**) and (**c**), the horizontal mirror symmetry and the C6 symmetries are broken, consistent with the symmetry-breaking behavior observed in the ARPES data from the perspective of the spectral weight distribution.

https://doi.org/10.1038/s41567-026-03205-7

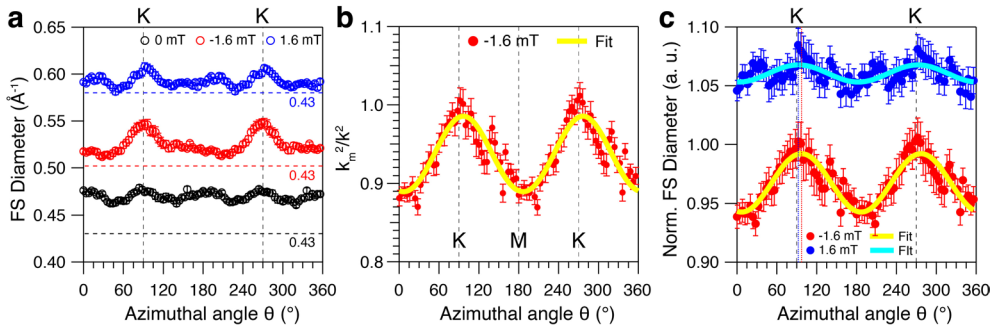

Extended Data Fig. 8 | Γ-pocket Fermi surface fitting based on the model of Methods Section F, Eq. (7). (**a**) Fermi pocket diameter as a function of the azimuthal angle obtained by fitting the radial MDCs without and with a magnetic field. The curves at -1.6 mT and 1.6 mT are offset for clarity with the reference lines shown for each. Error bars represent the standard deviation of the Lorentzian fits to the corresponding MDC peaks along different Fermi surface directions with 95% confidence interval. (**b**) Square of the Fermi momentum for -1.6 mT normalized by the zero field value overlaid with the fitting results using Eq. 7. Error bars are derived from the corresponding error bars in (**a**). (**c**) Fermi pocket diameter for -1.6 mT and 1.6 mT normalized by its zero-field value measured at 35 K. Error bars are derived from the corresponding error bars in (**a**). All curves are fitted with the function $A + B\cos(2(\theta + \pi))$. The red and blue dashed lines indicate the deviation of the long axes of the elliptical Fermi pockets away from the K point at -1.6 mT (6.9°) and 1.6 mT (2.3°), respectively.